

Attitude-Independent Magnetometer Calibration with Time-Varying Bias

John C. Springmann* and James W. Cutler†
University of Michigan, Ann Arbor, Michigan 48109

DOI: 10.2514/1.56726

A method is presented for on-orbit, attitude-independent magnetometer calibration that includes the effect of time-varying bias due to electronics onboard a spacecraft. The calibration estimates magnetometer scale factors, nonorthogonality, and constant as well as time-varying bias. The unique contribution of this paper is estimation of time-varying magnetometer bias due to nearby electronics. It is accomplished by including spacecraft telemetry in the measurement model and estimating constant parameters that map time-varying current to magnetometer bias. The calibration is demonstrated by application to flight data from the RAX-1 satellite and significantly reduces the uncertainty of off-the-shelf magnetometers embedded within the satellite and subject to spacecraft-generated fields. This method simplifies the satellite design process by reducing the need for booms and strict magnetic cleanliness, resulting in reduced satellite development time and cost. In addition to on-orbit magnetometers, the calibration method is applicable to air, ground, and water navigation.

I. Introduction

A METHOD is presented for attitude-independent, on-orbit magnetometer calibration that mitigates the effect of time-varying magnetic fields produced by electronics onboard a spacecraft. The calibration significantly increases the accuracy of measurements from magnetometers embedded within a satellite. Three-axis magnetometers are a common sensor on low-Earth-orbiting spacecraft because they are reliable, lightweight, have low power requirements, and have no moving parts [1]. They are typically used for attitude determination and scientific measurements. In this work, calibration was motivated by improved magnetometer-based attitude determination, but the calibration is applicable to other magnetometer-based sensing systems on a variety of platforms, such as air-, ground-, or water-based vehicles [2].

In general, three-axis magnetometer measurements are corrupted by both constant and time-varying sources of error. Time-invariant sources include hard iron errors, null shift errors, soft iron errors, scale factors, and nonorthogonality errors [3,4]. Hard iron error is a constant magnetic field bias that is caused by unwanted magnetic fields near the magnetometer, typically due to ferromagnetic (hard iron) materials. Null shift errors, also known as dc offset or zero bias, also result in magnetometer bias, but are inherent to the sensor. Soft iron errors result from materials that generate fields in response to externally applied fields (commonly called soft iron materials), affecting the gain of the magnetometer. Scale factor errors are inherent to the sensor and result from different sensitivities in each axis of the sensor. Nonorthogonality errors are due to angular deviation from a perfectly orthogonal three-axis configuration, and can be caused by manufacturing errors, thermal stress, or mechanical stress. Time-varying magnetometer errors are caused by nearby electronics: current-carrying wires create magnetic fields, resulting in a time-varying magnetometer bias.

The purpose of calibration is to quantify the statistical properties of the magnetometer errors [5,6]. Various algorithms exist to estimate

the time-invariant errors, which are captured by three general error types: bias, scale factors, and nonorthogonality. For example, TWOSTEP estimates magnetometer bias [7,8] and has been extended to estimate scale factors and nonorthogonality [9]. The first step is a centering approximation to provide an initial estimate of the calibration parameters, and the second step is a Gauss–Newton method to iteratively refine the parameters. In similar work, [10] uses a geometric approach to formulate the problem of compensating for magnetometer errors as estimation of parameters lying on an ellipsoid. A simpler method that uses least-squares minimization to estimate bias, scale factors, and nonorthogonality is developed in [3,4]. These algorithms [3,4,7–10] are batch methods, but real-time magnetometer correction can be implemented by uploading the calibration parameters to the spacecraft after the batch calibration is completed. Real-time implementations of [9] using nonlinear Kalman filtering techniques are developed in [11].

The above calibration techniques are attitude-independent, meaning no attitude knowledge is required for the calibration. This is critical because magnetometers can be used to estimate attitude, so attitude is generally not available before calibration. In lieu of knowledge of the vector components of the ambient magnetic field, attitude-independent calibration algorithms rely on knowledge of the magnitude of the expected geomagnetic field, which is obtained from a trusted sensor regarded as truth or a model such as the International Geomagnetic Reference Field (IGRF) [12]. The sensor calibration is typically carried out in a coordinate system attached to the magnetometer. However, the calibration methods presented in [10,13], an extension of [4], include an additional step to estimate the alignment of the magnetometer relative to the vehicle body frame.

The existing algorithms have been shown to accurately correct for constant sources of magnetometer error [4,9,10]. In practice, the time-varying bias caused by nearby electronics can result in additional magnetometer errors. Traditionally, this bias is mitigated by either using a boom to physically separate the magnetometer from the spacecraft, or by using design and manufacturing practices to minimize the influence of electronic components on magnetometers (for example, [14]). Such design practices increase the satellite development time and cost, and with the trend toward smaller spacecraft with reduced development times and costs [15–17], it may be impossible to physically separate a magnetometer from other spacecraft electronics.

In this paper, the work of Foster and Elkaim [4] is expanded to include time-varying bias in the calibration. The original contribution of this work is an attitude-independent, on-orbit method to estimate magnetometer bias caused by nearby electronics. This is accomplished by including measurements of spacecraft electric

Received 21 October 2011; revision received 27 December 2011; accepted for publication 28 December 2011. Copyright © 2012 by John C. Springmann and James W. Cutler. Published by the American Institute of Aeronautics and Astronautics, Inc., with permission. Copies of this paper may be made for personal or internal use, on condition that the copier pay the \$10.00 per-copy fee to the Copyright Clearance Center, Inc., 222 Rosewood Drive, Danvers, MA 01923; include the code 0731-5090/12 and \$10.00 in correspondence with the CCC.

*Ph.D. Candidate, Department of Aerospace Engineering; jspringm@umich.edu.

†Assistant Professor, Department of Aerospace Engineering; jwcutler@umich.edu.

currents in the sensor model and estimating constant parameters that map time-varying current to magnetometer bias. In similar work, Kim et al. [18] estimate the bias resulting from a magnetic torque coil by expanding the model of [9] to include the magnetic dipole moment produced by the torque coil. Our method is general in that the bias caused by any electronic component can be estimated. The current measurements used in the calibration are typically already part of spacecraft health monitoring, so no additional sensors need to be added during design. This method simplifies the spacecraft design process by replacing magnetic cleanliness, magnetometer location, and preflight calibration requirements with on-orbit calibration. The effectiveness of the calibration is demonstrated by application to flight data from the RAX-1 satellite.

The remainder of this paper is organized as follows. In Sec. II, time-invariant calibration methods are reviewed before extending the calibration to include time-varying bias in Sec. III. In Sec. IV, both the time-invariant and time-varying calibrations are applied to on-orbit data, and the improvement over time-invariant methods, convergence of the calibration parameters, and accuracy of the calibration are discussed. Conclusions are given in Sec. V.

II. Review of Existing Methods

The new method to estimate time-varying magnetometer bias is an extension of an existing magnetometer calibration algorithm that estimates the time-invariant errors [4]. For completeness, the existing method is reviewed before presenting the extension.

In general, there are two steps in sensor calibration: (1) model the sensor, and (2) estimate parameters of the model. The three-axis sensor model that includes the time-invariant errors is [4]

$$\tilde{B}_x = aB_x + x_0 + \eta_x \quad (1)$$

$$\tilde{B}_y = b(B_y \cos(\rho) + B_x \sin(\rho)) + y_0 + \eta_y \quad (2)$$

$$\begin{aligned} \tilde{B}_z &= c(B_x \sin(\lambda) + B_y \sin(\phi) \cos(\lambda) \\ &\quad + B_z \cos(\phi) \cos(\lambda)) + z_0 + \eta_z \end{aligned} \quad (3)$$

where \tilde{B}_x , \tilde{B}_y , and \tilde{B}_z are the measured magnetic fields along each axis of the sensor; B_x , B_y , and B_z are the components of the ambient geomagnetic field resolved in a perfectly orthogonal sensor frame; the magnetometer errors are parametrized by scale factors in each axis (a , b , c), constant bias in each axis (x_0 , y_0 , z_0), and the sensor nonorthogonality angles (ρ , λ , ϕ) modeled with the geometry shown in Fig. 1; and η_x , η_y , and η_z are zero-mean measurement noise in each axis.

The purpose of the calibration is to estimate a , b , c , x_0 , y_0 , z_0 , ρ , λ , and ϕ , herein referred to as the calibration parameters. There are two

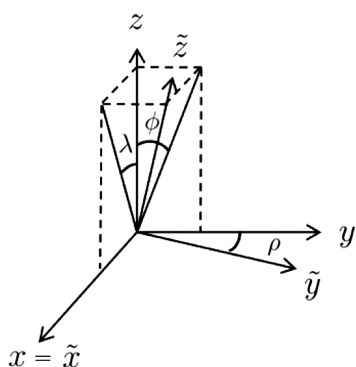


Fig. 1 The convention used to define the sensor nonorthogonality by the angles ρ , ϕ , and λ . \tilde{x} , \tilde{y} , and \tilde{z} represent the actual sensor axes, and x , y , and z denote the axes of the orthogonal frame. The x -axis of the true and orthogonal frames are coincident, and the y -axis is in the \tilde{x} - \tilde{y} plane. Figure adapted from [25].

assumptions in the magnetometer model: the magnetometer and the sources of error are rigidly attached to the same vehicle, and responses to soft iron materials are linear (without hysteresis), which corresponds to the use of linear scale factors a , b , and c .

The magnetometer model captures the total bias, linear scaling, and nonorthogonality errors, but it is not possible to mathematically separate each individual error source. For example, both hard iron error and null shift error contribute to the bias in each magnetometer axis, x_0 , y_0 and z_0 . Similarly, both soft iron and scaling inherent to the sensor contribute to the scale factor errors, a , b , and c , and both soft iron errors and physical nonorthogonality errors are manifested in the angles ρ , λ , and ϕ . The mapping from soft iron error to nonorthogonality occurs because soft iron can cause cross-axis gain terms. For example, an ambient field in the z -axis could cause a soft-iron-induced magnetic field in the x -axis. Even though this nonobservability of physical error sources exists, estimation of the total bias, linear scaling, and nonorthogonality parameters is sufficient to correct the magnetometer measurements [4].

The calibration parameters are observable through the magnetic field magnitude. The calibration is independent of spacecraft attitude since only the field magnitude, rather than vector components, is required. To formulate the minimization problem, Eqs. (1–3) are rewritten to give the geomagnetic field components as functions of the measurements and calibration parameters. The squared magnitude of the measured geomagnetic field is then given by

$$B^2 = B_x^2 + B_y^2 + B_z^2 = f(\tilde{B}_x, \tilde{B}_y, \tilde{B}_z, a, b, c, x_0, y_0, z_0, \rho, \phi, \lambda) \quad (4)$$

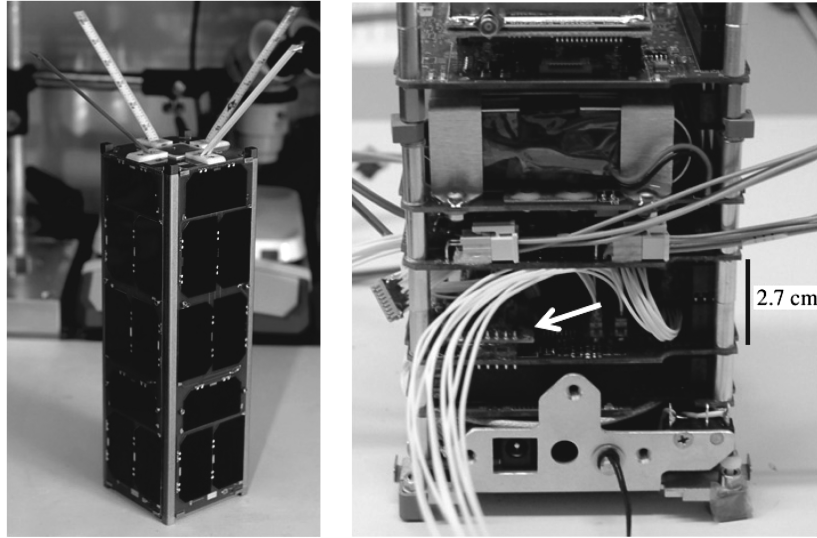
The expected magnetic field magnitude, B_E , is obtained from a model of the geomagnetic field, such as the IGRF [12], coupled with knowledge of spacecraft location. The calibration parameters are estimated by minimizing the difference between measured and expected geomagnetic field magnitude, $\min(B_E^2 - B^2)$.

There are various methods available to carry out the minimization and estimate the calibration parameters. In [4], least-squares minimization is used. If the geomagnetic field magnitude is constant, such as during ground-based testing in a fixed location, Eq. (4) can be rewritten in a linear form using intermediate variables that are functions of the calibration parameters. This facilitates the use of batch linear least squares to estimate the parameters [4]. If the geomagnetic field is time-varying (the vehicle is moving sufficient distances through the geomagnetic field), the minimization can be iteratively processed by a nonlinear least-squares batch algorithm.

In other work, maximum likelihood estimation, rather than least-squares minimization, is used to estimate the calibration parameters [9,10]. Reference [11] uses nonlinear Kalman filtering to recursively estimate the parameters. Although least-squares minimization is suboptimal, it still produces very good estimates of the calibration parameters [4]. In our calibration that includes time-varying bias, we use an iterative nonlinear least-squares minimization rather than maximum likelihood estimation because it is simpler and provides sufficient performance for our application, as we will demonstrate in Sec. IV.

III. Inclusion of Time-Varying Bias

Time-varying bias due to onboard electronics is estimated by including telemetered spacecraft currents in the magnetometer model. Since current-carrying wires create magnetic fields, we include current measurements in the magnetometer model and estimate constant parameters that map the time-varying current to magnetometer bias. In general, the magnetic field produced by a current-carrying wire is a function of the wire geometry, the current magnitude, and the relative orientation and location of interest. It is given by the Biot–Savart law, which can be integrated in closed form for only specific wire configurations, such as a circular loop or straight infinite length [19]. However, assuming that the wire geometry and the location and orientation of the magnetometer relative to the wire are constant, the magnetic field produced at the location of the magnetometer can be written as a linear function of the current, where a single coefficient maps the current to the resulting



a) The flight-ready satellite. The physical dimension are $30 \times 10 \times 10 \text{ cm}^3$.

b) The inside of the lower portion of the satellite is shown. The arrow points to the PNI MicroMag3 magnetometer. The circuit board located directly above the magnetometer is the satellite power regulation system.

Fig. 2 The RAX-1 satellite is shown both fully and partially integrated.

magnetic field component. This yields the following magnetometer model:

$$\tilde{B}_x = aB_x + x_0 + \sum_{i=1}^c s_{i,\tilde{x}} \tilde{I}_i + \eta_x \quad (5)$$

$$\tilde{B}_y = b(B_y \cos(\rho) + B_x \sin(\rho)) + y_0 + \sum_{i=1}^c s_{i,\tilde{y}} \tilde{I}_i + \eta_y \quad (6)$$

$$\begin{aligned} \tilde{B}_z &= c(B_x \sin(\lambda) + B_y \sin(\phi) \cos(\lambda) + B_z \cos(\phi) \cos(\lambda)) \\ &+ z_0 + \sum_{i=1}^c s_{i,\tilde{z}} \tilde{I}_i + \eta_z \end{aligned} \quad (7)$$

The model is identical to Eqs. (1–3) with one additional term in each axis: $\sum_{i=1}^c s_{i,j} \tilde{I}_i, j \in \{\tilde{x}, \tilde{y}, \tilde{z}\}$, where $s_{i,j}$ is the coefficient that maps the i -th current measurement \tilde{I}_i to the magnetic field in the j -th magnetometer axis, and c is the total number of current measurements included in the model. Even though current measurements are required for the calibration, onboard current sensors are typically part of spacecraft health-monitoring, so inclusion of the current measurements in the calibration does not necessarily require current sensors to be added to a spacecraft solely for the purpose of calibration. The model does not require any knowledge of the layout of the electronic components; the calibration requires only current measurements, magnetometer measurements, and the expected magnitude of the geomagnetic field.

Care must be taken when selecting current telemetry to include in the magnetometer model. Use of the model is effective only when the included currents affect the magnetometers. If not, physically meaningful mapping coefficients $s_{i,j}$ are not observable, and the accuracy of the calibration will be degraded. Evidence to decide which current measurements to include is discussed in Sec. IV.C. Additionally, the current measurements must be linearly independent to obtain unique mapping coefficients. If linearly dependent measurements are used, the unobservability will be manifested by a rank deficient Jacobian matrix that is required for the estimation [$\frac{\partial f(\tilde{B}, \tilde{I}, x)}{\partial x}$, see Eq. (8)].

In the magnetometer model of Eqs. (5–7), there are $9 + 3c$ calibration parameters, and the parameters are estimated in the same

manner described in the previous section: the difference between the measured and expected geomagnetic field magnitude is minimized. Nonlinear least squares is used for the minimization. Also known as Gaussian least-squares differential correction, this method is a generalization of Newton's root solving method that iteratively minimizes the loss function J [20], given by

$$J = \frac{1}{2} [\mathbf{B}_E^2 - \mathbf{f}(\tilde{\mathbf{B}}, \tilde{\mathbf{I}}, \mathbf{x})]^T [\mathbf{B}_E^2 - \mathbf{f}(\tilde{\mathbf{B}}, \tilde{\mathbf{I}}, \mathbf{x})] \quad (8)$$

In Eq. (8), \mathbf{B}_E^2 is an $m \times 1$ vector of the expected field magnitudes squared, where m is the number of measurements, and $\mathbf{f}(\tilde{\mathbf{B}}, \tilde{\mathbf{I}}, \mathbf{x})$ is an $m \times 1$ vector of the geomagnetic field magnitudes squared as a function of the $m \times 3$ magnetometer measurements $\tilde{\mathbf{B}}$, the $m \times c$ current measurements $\tilde{\mathbf{I}}$, and the calibration parameters \mathbf{x} at the current iteration. The loss function J is quartic, which can result in the convergence to incorrect local minima. In some minimization techniques, such as that used in [7], centering is used to reduce the loss function from quartic to quadratic. In nonlinear least squares, $\mathbf{f}(\tilde{\mathbf{B}}, \tilde{\mathbf{I}}, \mathbf{x})$ is linearized at each iteration, which results in a quadratic loss function without the need for centering. A derivation of nonlinear least squares is not included here, but rather, the reader is directed to existing references ([20]). In general, convergence of nonlinear least squares is not guaranteed, but no problems have been found with converging to a single set of parameters. This is discussed further in Sec. IV.D.

IV. Application to Flight Data

The calibration algorithm has been tested through application to both simulated and actual on-orbit data. In this section, the algorithm is applied to on-orbit data from the RAX-1 satellite, a nanosatellite that uses magnetometers for attitude determination. In Sec. IV.A, the on-orbit data and use of the IGRF are discussed. In Sec. IV.B, an existing time-invariant calibration method is applied to the on-orbit data, and the results demonstrate the need for calibration with time-varying bias. Application of the time-varying calibration is presented in Sec. IV.C, convergence of the calibration parameters is discussed in Sec. IV.D, and accuracy of the calibration is discussed in Sec. IV.E.

Table 1 The time difference between the epochs of the TLEs used and the time of the magnetometer data sets

Data set	Time difference, days
Dec. 1	2.24
Dec. 15	0.16
Dec. 30	1.08

A. RAX-1 and IGRF Data

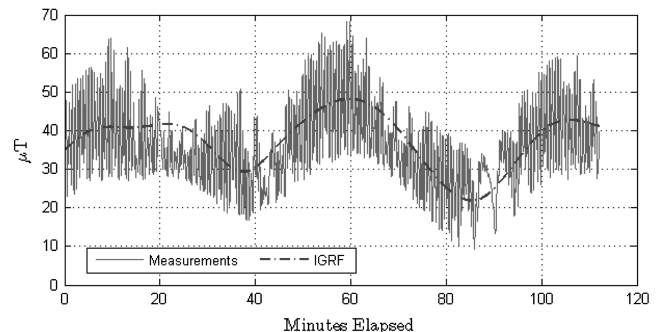
RAX-1 [21,22], shown in Fig. 2a, is a CubeSat (a specific satellite form-factor) with physical dimensions of $30 \times 10 \times 10 \text{ cm}^3$ and mass of 2.8 kg. It is in a 650 km altitude, 72 deg inclination circular orbit. Commercial off-the-shelf magnetometers are used in conjunction with photodiodes and a three-axis rate gyroscope for attitude determination [23]. The magnetometers are embedded within the satellite and subject to spacecraft-generated magnetic fields. The data used in this section are from one of the onboard three-axis magnetometers, a PNI Sensor Corporation MicroMag3, which is shown in Fig. 2b. The sensor resolution is 128 nanotesla (nT) in each axis. From preflight testing, the noise floor of the stand-alone sensor was found to be below the sensor resolution, so the resolution itself provides a metric for the effectiveness of the on-orbit calibration.

The international geomagnetic reference field (IGRF) [12] is used for the expected field magnitude. The IGRF is a geomagnetic field model that provides geomagnetic field components in an Earth-fixed frame as a function of location. Spacecraft position is obtained from a two-line element (TLE) set. The time differences between the TLE epochs and each data set discussed in this section are given in Table 1. AGI's satellite tool kit (STK)[‡] was used to obtain IGRF data from TLEs. The TLEs are propagated using STK's SGP4 propagator, and the complete (order 13, degree 13) eleventh generation IGRF model [12] is built in to STK, so the expected field magnitude corresponding to each sensor reading is obtained directly from STK based on the time of the sensor reading and the TLE.

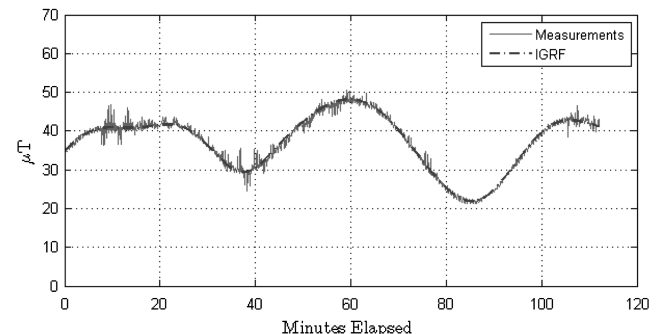
The accuracy of the expected field magnitude is a critical aspect of the magnetometer calibration. Accuracy of the IGRF is approximately 10 nT during nominal space weather conditions [24], which is better than typical attitude-grade magnetometers, and is an order of magnitude better than the resolution of the magnetometer used in this section. Space weather conditions must be considered since space weather affects the geomagnetic field, and the calibration should only be carried out when the geomagnetic field fluctuations are sufficiently below the resolution of the magnetometer. The Kp index[§], a measure of geomagnetic field activity, was less than 2+ for each data set used for the calibration. This indicates that geomagnetic field fluctuations are expected to be below 20 nT[¶] and validates the assumption that the IGRF will provide accurate data for the time periods of interest.

B. Calibration with Time-Invariant Parameters

To demonstrate the need for calibration that includes time-varying bias, time-invariant calibration is first applied to the on-orbit data before application of the new algorithm. Figure 3 shows 112 min of on-orbit magnetometer data taken at approximately 1 Hz on 1 December 2010. Figure 3a shows the raw, uncalibrated magnitude of the measured data, and is overlaid with the expected field magnitude. The calibration method discussed in Sec. II is applied to estimate the time-invariant errors, and the magnitude of the corrected measurements are shown in Fig. 3b. Compared with the raw data of



a) Magnitude of the raw, uncalibrated measurements (μT) overlaid with the expected field magnitude using the IGRF model.



b) Magnitude of the measurements after correcting for timeinvariant errors (μT). The differences between the measured and IGRF magnitudes are shown in Figure 4.

Fig. 3 Data from the RAX-1 PNI MicroMag3 magnetometer. The x-axis of each plot shows time elapsed since the start of the data set, 1 Dec. 2010 08:30:46 UTC.

Fig. 3a, the measured magnitude is closer to the expected magnitude, but there are still discrepancies of up to 23% of the expected field magnitude. The difference between the corrected measured magnitude and the expected field magnitude is shown in Fig. 4. In Fig. 4a, an indicator is overlaid to show when the solar panels are illuminated and generating current. The indicator is based on sun sensor readings. There is a clear increase in the magnetometer errors when the satellite is in the sun, which suggests that currents flowing in the solar panels are affecting the magnetometer. A histogram of the differences is shown in Fig. 4b.

C. Application of Time-Varying Calibration

The model used to estimate time-varying bias [Eqs. (5–7)] can include any number of current measurements. Data presented in Fig. 3 suggest that currents produced by the solar panels degrade the magnetometer measurements. There are four body-mounted solar panels on RAX-1, and measurements of the current in each panel are included. From further experimentation with the on-orbit data, a fifth element, the current drawn from the battery, has been found to degrade the measurements [25]. Therefore, these five current measurements are included in the magnetometer model.

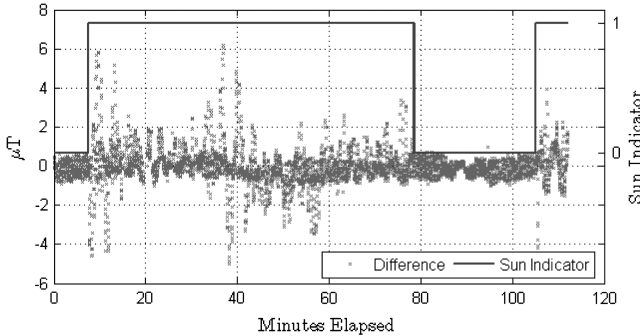
For the datasets presented in this paper, the current and magnetic sensors throughout the spacecraft were sampled simultaneously. In general, the frequency of sensor sampling is mission dependent: magnetometer and current sensors can be sampled at different rates based on the scientific and engineering requirements. The model of Eqs. (5–7) assumes that the current measurements were taken at the same time as the magnetometer measurements. If not, interpolation could be used as an approximation, but this will degrade the results. For general use of this algorithm, the ability to sample sensors simultaneously for the purposes of calibration should be considered in the design phase of the spacecraft.

The results of the calibration are shown in Fig. 5. Figure 5a shows the magnitude of the corrected measurements overlaid with the expected field magnitude, Fig. 5b shows the difference between

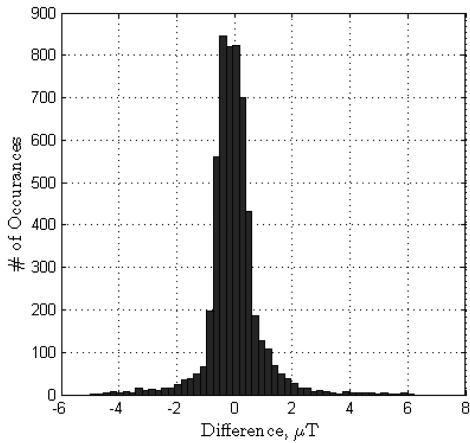
[‡]<http://www.agi.com/products/by-product-type/applications/stk/> [retrieved Sept. 2011].

[§]Kp index retrieved from the NOAA National Geophysical Data Center, http://www.ngdc.noaa.gov/stp/geomag/kp_ap.html [retrieved Sept. 2011].

[¶]The approximate magnetic field fluctuations as a function of Kp index are provided by the NOAA Space Weather Prediction Center, <http://swpc.noaa.gov/info/Kindex.html> [retrieved Dec. 2011].



a) The difference (μT) versus time. The sun indicator takes the value of one when RAX-1 is in the sun, and zero when in eclipse, which shows when the solar panels are illuminated and generating current.



b) A histogram of the differences (μT).

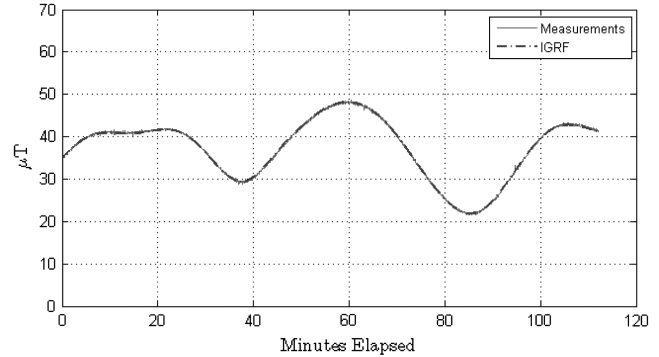
Fig. 4 Difference between the magnitude of the corrected measurements using time-invariant calibration, and the expected field magnitude, as shown in Fig. 3b.

the measured and expected magnitudes, and Fig. 5c is a histogram of the difference. Figures 5a and 5b show the significant improvement of the magnetometer data compared with the corresponding time-invariant calibration results shown in Figs. 3b and 4a. The root mean squared error (RMSE) of the measurements after calibration for time-invariant errors is 903 nT, where error is defined as the difference between the expected magnitude and the magnitude of the corrected measurements. After calibration with time-varying bias, the RMSE is reduced to 174 nT, an improvement factor of 5.2. This corresponds to an order of magnitude improvement in angular accuracy. Accuracy is discussed further in Sec. IV.D.

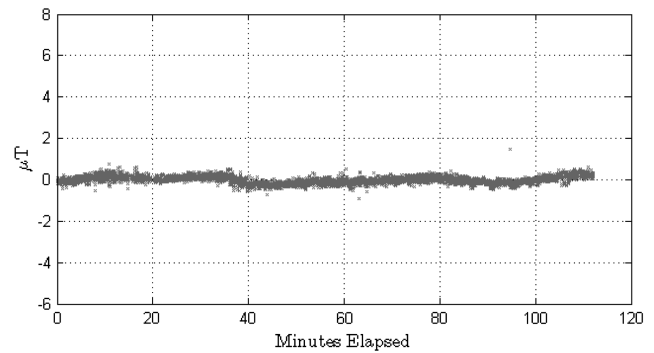
The resolution of the raw magnetometer measurements is 128 nT along each axis. The resolution of the corrected sensor readings in the orthogonal frame is transformed by the scale factors and nonorthogonality angles. After transformation of the 128 nT resolution with the calibration parameters, the resolution of the calibrated sensor is 144, 143, and 111 nT along the x , y , and z axes, respectively. This results in a 231 nT resolution on the magnitude of the corrected measurements. The RMSE of the calibrated data is only 174 nT, which is below the sensor resolution of 221 nT and indicates that the accuracy of the calibrated measurements has approached the fundamental accuracy limit of the sensor.

D. Convergence

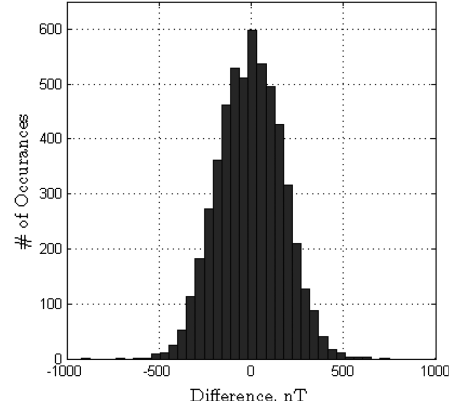
The calibration parameters are estimated using nonlinear least-squares minimization as described in Sec. III. An initial estimate of the calibration parameters is required to begin the iterative minimization, and in general, convergence to a global minimum is not guaranteed. A Monte Carlo simulation using 1000 different initial conditions was used to investigate the convergence. The initial



a) The magnitude of the corrected measurements (μT) versus time (minutes). The magnitude of the expected magnetic field is overlaid.



b) Difference between the corrected measured field magnitude and the expected magnitude (μT).



c) Histogram of the difference between the measured and expected magnitudes (nT). There are 5,405 total data points.

Fig. 5 Results of the calibration to estimate both constant errors and time-varying magnetometer bias.

conditions were uniformly distributed over the ranges shown in the second row of Table 2. The parameter estimates from each trial converged to the single local minimum shown in the third row of the table. The tolerance used in the minimization is

$$|\Delta y_l - \Delta y_{l-1}| < 1 \text{ nT}^2 \quad (9)$$

where l is the iteration number and

$$\Delta y_l = \frac{1}{m} \sum_{k=1}^m [B_{E,k}^2 - f(\tilde{\mathbf{B}}_k, \tilde{\mathbf{I}}_k, \mathbf{x}_l)] \quad (10)$$

is the mean difference between the expected and measured geomagnetic field magnitudes squared. In Eq. (10), the quantity $B_{E,k}^2 - f(\tilde{\mathbf{B}}_k, \tilde{\mathbf{I}}_k, \mathbf{x}_l)$ is defined as in Eq. (8), and k is the data index. Qualitatively, the tolerance of Eq. (9) means that the mean difference

Table 2 The range of uniformly distributed initial conditions used in the Monte Carlo simulations (row two) and the final estimate of the calibration parameters (row three), with 15 total mapping coefficients, $s_{i,j}$, and the range of the final coefficients given rather than each individual parameter for simplicity

Parameter	a	b	c	$x_0, \mu\text{T}$	$y_0, \mu\text{T}$	$z_0, \mu\text{T}$	ρ, deg	ϕ, deg	λ, deg	$s_{i,j}, \mu\text{T}/\text{mA}$
Range	-4–4	-4–4	-4–4	-20–20	-20–20	-20–20	-20–20	-20–20	-20–20	-1–1
Estimate	0.89	0.90	1.13	-0.69	9.91	-7.70	-1.04	-3.97	5.02	-0.02–0.01

between the expected and measured geomagnetic field magnitudes squared changes by less than 1 nT² with each iteration. Although 1 nT is below the resolution of the measurements, the expected geomagnetic field magnitude is obtained from a continuous model, so Δy can take any value. From the Monte Carlo simulations, a 1 nT² tolerance was found to be sufficient: the parameter estimates from each trial converged to a single local minimum within seven iterations. This demonstrates that there are no problems with convergence and suggests that a global minimum exists. A formal study of convergence is left for future work.

E. Calibration Accuracy

In this subsection, the accuracy of both the corrected magnetic field measurements and the calibration parameters is discussed.

The direction of all possible measurements taken by a three-axis vector sensor can be represented by a sphere. That is, if an ideal (perfectly calibrated, no noise) three-axis magnetometer is rotated in a constant magnetic field, the measurements, plotted in three

dimensions, lie on a sphere. This sphere is referred to as the *attitude sphere*. Data from an uncalibrated magnetometer form an ellipsoid [4,10]. Estimates of the calibration parameters are most accurate if the measurements used in the calibration are distributed over the entire surface of the ellipsoid [4,10], and this is discussed further in the Appendix.

Figure 6a shows the components of the normalized measurements after calibration. This is the same data as Figs. 3–5. For this data set, the measurements are distributed over the entire attitude sphere. The components from two other data sets, taken 15 December and 30 December 2010, are shown in Figs. 6b and 6c. RAX-1 uses a passive magnetic control system, which gradually aligns the satellite with Earth's magnetic field. This is evident in Fig. 6. On 1 December, the satellite is still tumbling after deployment from the launch vehicle. As time passes, the satellite aligns with the geomagnetic field, resulting in the reduced sphere coverage seen in Figs. 6b and 6c.

Nine of the 24 calibration parameters estimated from each data set are shown in Table 3. There is variation between the parameters, and

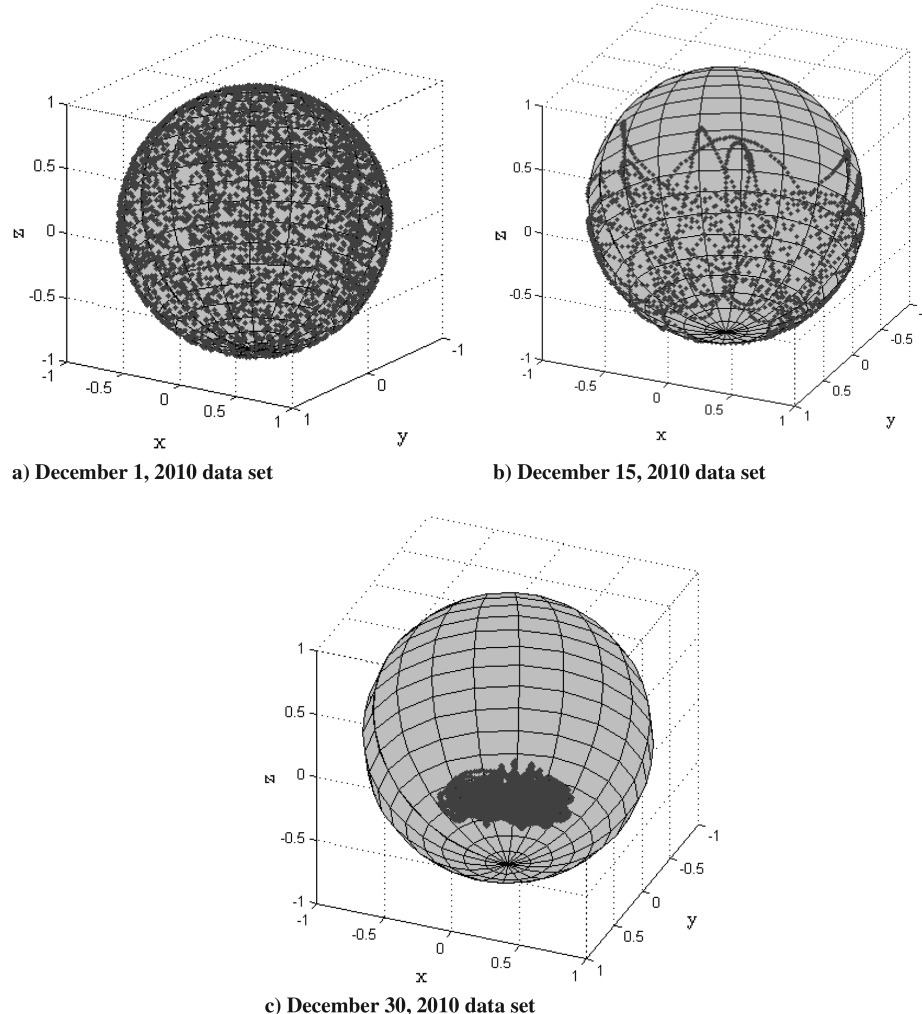


Fig. 6 The normalized vector components of the corrected measurements plotted in three dimensions on top of a unit sphere in the body frame for each data set, which shows the coverage of the *attitude sphere*.

Table 3 Estimates of the calibration parameters for each data set, with 9 of the 24 parameters shown and the remaining omitted from the table for simplicity

Data set	<i>a</i>	<i>b</i>	<i>c</i>	$x_0, \mu\text{T}$	$y_0, \mu\text{T}$	$z_0, \mu\text{T}$	ρ, deg	ϕ, deg	λ, deg
1 Dec.	0.890	0.910	1.130	-0.687	9.909	-7.700	-1.039	-3.974	5.019
15 Dec.	0.893	0.913	1.136	-0.581	10.014	-7.419	-1.085	-4.310	5.178
30 Dec.	0.900	0.911	1.170	-0.944	9.478	-6.220	-1.437	-4.160	4.498

Table 4 The RMSE (nT) of the corrected measurements after calibration using the parameter estimates from each data set, with measurements from the data sets listed in the left column corrected using parameters from the data sets listed across the top

Corrected measurements	Calibration parameters used		
	1 Dec.	15 Dec.	30 Dec.
1 Dec.	174	320	1074
15 Dec.	219	160	490
30 Dec.	210	200	153

Table 5 The RMSE (nT) of the corrected measurements after time-invariant calibration using the parameter estimates from each data set, analogous to Table 4 but the calibration method is the existing time-invariant method described in Sec. II, with measurements from the data sets listed in the left column corrected using parameters from the data sets listed across the top

Corrected measurements	Calibration parameters used		
	1 Dec.	15 Dec.	30 Dec.
1 Dec.	903	2064	3351
15 Dec.	792	725	1266
30 Dec.	677	825	391

to investigate the accuracy of the parameters, each set of measurements is corrected with each set of calibration parameters. The resulting RMSEs after calibration are given in Table 4. The table shows the RMSE after each set of measurements is corrected by each set of calibration parameters. For example, the RMSE of the 1 December corrected measurements using the parameters estimated from the 1 December measurements is 174 nT. The RMSE of the 15 December corrected measurements using the parameters estimated from the 30 December measurements is 490 nT. Table 5 is analogous to Table 4, but the measurements in Table 5 are corrected using the time-invariant method described in Sec. II. Table 5 is included to demonstrate the improvement of the new calibration method relative to existing methods.

There are two significant aspects of the errors shown in Table 4. First, the RMSEs of the 1 December data set corrected with parameters from the 1 December, 15 December, and 30 December data sets (first row) indicate that parameter estimates from the 1 December data set are most accurate. Additionally, the fact that the RMSEs of each data set corrected with the 1 December parameters are all within one sensor resolution (first column) indicates that the parameters are constant over time.

A second approach is taken to study the differences in the parameters of Table 3. The Fisher information matrix [20] is used to approximate the lower bound on the covariance of the calibration parameters. This is shown in the Appendix. As discussed in the Appendix, the lower bound is optimistic, but it quantifies the decrease in observability of the parameters as the sphere coverage decreases. This decrease in observability is why there are differences in the calibration parameters estimated from each data set.

The resulting accuracy of the corrected measurements (within one sensor resolution) and the observability study using the Fisher information matrix indicate that the calibration parameter estimates from the 1 December data set are accurate. Through application to flight data, it has been shown that the calibration with time-varying bias significantly improves the accuracy of the calibration. For example, the RMSE of the 15 December data set after correction with constant parameters obtained from the 1 December data set is 792 nT. With time-varying calibration, this is improved to 219 nT, an angular improvement** from 1.3 to 0.36 deg in an ambient field of 35 μT .

V. Conclusions

A method for on-orbit, attitude-independent magnetometer calibration that includes time-varying bias due to nearby electronics has been developed. Existing time-invariant calibration methods have been extended by including current measurements in the sensor model, and the resulting calibration method estimates both time-invariant errors and time-varying bias due to onboard electronics. The time-varying bias is estimated by mapping current to magnetometer bias through constant parameters. The calibration parameters are estimated using an iterative least-squares minimization, and only the magnetometer measurements, current measurements, and the expected magnitude of the geomagnetic field are required for the calibration.

The usefulness of the calibration has been demonstrated by application to on-orbit data. In application to the RAX-1 satellite, the calibration successfully mitigates magnetometer bias due to the satellite power system. The calibration improved the RMSE of magnetometer measurements from 792 to 219 nT, corresponding to an order of magnitude increase in angular accuracy.

Traditionally, time-varying bias is mitigated by either using a boom to physically separate the magnetometer from the spacecraft, or by using design and manufacturing practices to minimize the influence of electronic components on magnetometers. Such design practices increase design time and cost, and physical separation of a magnetometer from onboard electronics may not be possible as satellites continue to decrease in size. The algorithm presented in this work effectively replaces such design practices with improved processing of the sensor measurements. The algorithm uses current sensors throughout the spacecraft that are sampled at the same time as the magnetometers, so inclusion of current sensors and the ability to sample the sensors simultaneously for the purpose of calibration should be considered in the design phase of the vehicle. Although the calibration is a batch method, parameters can be uploaded to the spacecraft for real-time magnetometer correction, and real-time implementation will be developed in future work. The calibration has been applied to satellite-based magnetometers in this work, but this algorithm is applicable to other magnetometer applications on a variety of platforms.

Appendix: Uncertainty of the Calibration Parameters

The Fisher information matrix [20] is used to investigate the degradation of the calibration accuracy as the coverage of the attitude sphere decreases. For a linear estimation problem of the form $\tilde{\mathbf{y}} = \mathbf{H}\mathbf{x} + \mathbf{v}$, where $\tilde{\mathbf{y}}$ is the $m \times 1$ measurement vector, \mathbf{x} is the $n \times 1$

**To approximate the angular accuracy, we assume the error is orthogonal to the magnetic field vector.

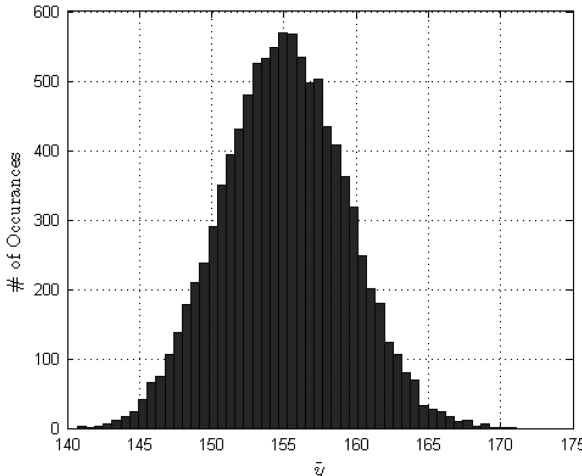


Fig. A1 Histogram of \tilde{y} calculated from 10,000 random sensor measurements with Gaussian distribution and the calibration parameters for the 1 December data set, shown in Table 3. The standard deviations used are $\sigma_x = \sigma_y = \sigma_z = 128$ nT, and $\sigma_1 = \dots = \sigma_5 = 5$ mA.

state vector, and \mathbf{v} is the $m \times 1$ zero mean measurement noise vector of covariance R , the Fisher information matrix is

$$F = H^T R^{-1} H \quad (\text{A1})$$

The Cramér—Rao inequality provides a lower bound for the state covariance matrix, P [20]:

$$P \geq F^{-1} \quad (\text{A2})$$

The magnetometer parameter estimation is linearized to use this inequality to determine the approximate lower bound on the uncertainty of the calibration parameters. The measurement in the calibration problem, the squared magnitude of the corrected magnetic field measurements, is given by

$$\tilde{\mathbf{y}} = \mathbf{f}(\tilde{\mathbf{B}}, \tilde{\mathbf{I}}, \mathbf{x}) \quad (\text{A3})$$

as in Eq. (8). H is approximated by linearizing at the final state estimate, \mathbf{x}_f :

$$H = \left. \frac{\partial \mathbf{f}(\tilde{\mathbf{B}}, \tilde{\mathbf{I}}, \mathbf{x})}{\partial \mathbf{x}} \right|_{\mathbf{x}_f} \quad (\text{A4})$$

The raw measurements for a single point in time are

$$\tilde{\mathbf{y}}' = [\tilde{B}_x \quad \tilde{B}_y \quad \tilde{B}_z \quad \tilde{I}_1 \quad \tilde{I}_2 \quad \tilde{I}_3 \quad \tilde{I}_4 \quad \tilde{I}_5]^T \quad (\text{A5})$$

where \tilde{B}_x , \tilde{B}_y , and \tilde{B}_z are the magnetometer measurements [modeled in Eqs. (5–7)], and \tilde{I}_1 – \tilde{I}_5 are the five current measurements used in the calibration.

Let the covariance of the error in $\tilde{\mathbf{y}}$ be given by R and the covariance of $\tilde{\mathbf{y}}'$ be given by $R_{\tilde{B}, \tilde{J}}$. It is assumed that the sensor measurement covariance is a diagonal matrix of the variances of each measurement

$$R_{\tilde{B}, \tilde{J}} = \text{diag}[\sigma_x^2 \quad \sigma_y^2 \quad \sigma_z^2 \quad \sigma_1^2 \quad \sigma_2^2 \quad \sigma_3^2 \quad \sigma_4^2 \quad \sigma_5^2] \quad (\text{A6})$$

Since $\tilde{\mathbf{y}}$ is a nonlinear function of the sensor measurements and calibration parameters, it is not necessarily a Gaussian random vector. A Monte Carlo simulation was performed to investigate the probability density function of $\tilde{\mathbf{y}}$. $\tilde{\mathbf{y}}$ was calculated using 10,000 random Gaussian distributed sensor measurements and the calibration parameters from the 1 December data set, given in Table 3. The histogram of the results is shown in Fig. A1. This histogram indicates that it is reasonable to assume that the error in $\tilde{\mathbf{y}}$ is a Gaussian random vector. Therefore, the covariance matrix R is calculated after linearization as it would be for linear systems:

$$R = \text{diag}[R_1 \quad \dots \quad R_m] \quad (\text{A7})$$

where

$$R_i = [\mathbf{f}(\tilde{\mathbf{B}}_i, \tilde{\mathbf{I}}_i, \mathbf{x})] R_{\tilde{B}, \tilde{J}} [\mathbf{f}(\tilde{\mathbf{B}}_i, \tilde{\mathbf{I}}_i, \mathbf{x})]^T \quad (\text{A8})$$

The necessary tools to approximate the Fisher information matrix are now available. From preflight testing, the uncertainty in the magnetometer measurements was found to be less than the resolution of the sensor, so the standard deviation is approximated by the resolution, 128 nT in each axis. The expected uncertainty of the IGRF magnitude is an order of magnitude less than the sensor resolution, so it is not explicitly included in the magnetic field uncertainty. The uncertainty of the current sensors throughout the spacecraft was not thoroughly characterized before flight. The standard deviation is assumed to be 5 mA (the resolution is 1 mA). Using these standard deviations, the estimated lower bound of the 3- σ values of the calibration parameters, obtained from the diagonal elements of the state covariance matrix of Eq. (A2), are given in Table A1.

The 3- σ values are optimistic. The Cramér—Rao inequality provides a lower bound of the state covariance, not the actual covariance. In the magnetometer calibration, nonlinear least-squares minimization was used, but it is not an optimal estimator and does not consider the probability density function of the errors. This, coupled with the fact that linearized approximations of nonlinear functions were used, indicates that the actual 3- σ values of our state estimates are worse than the lower bound. This is confirmed by observing that the parameters estimated from each data set do not match within the 3- σ bound. However, the lower bound provides insight into the accuracy of the parameters and the relationship to coverage of the attitude sphere. The lower bound of the 3- σ values increases as the coverage of the attitude sphere decreases (sphere coverage for each data set is shown in Fig. 6). This is expected, and is an example of one metric that quantifies the decrease in observability of the calibration parameters as the sphere coverage decreases. Ultimately, if the data points were available from less than n independent data points on the sphere, then H would become rank deficient and the parameters would be unobservable.

Acknowledgments

The authors thank Pierre Kabamba and Sara Spangelo for comments on this paper, and thank Ben Kempke and the other students in the Michigan Exploration Laboratory for their support of this work. This research is a subset of a larger magnetometer calibration project done in collaboration with Creare, Inc., and funded by the U.S. Air Force Research Laboratory contract FA9453-10-C-0056. Additional funding came from the Department of

Table A1 Approximate lower bound of the 3- σ values of the calibration parameter estimates for each data set, with 9 of the 24 parameters shown and the remaining omitted from the table for simplicity

Data set	a	b	c	$x_0, \mu\text{T}$	$y_0, \mu\text{T}$	$z_0, \mu\text{T}$	ρ, deg	ϕ, deg	λ, deg
1 Dec.	4.0×10^{-4}	4.2×10^{-4}	4.6×10^{-4}	0.015	0.015	0.019	0.041	0.040	0.040
15 Dec.	8.8×10^{-4}	1.1×10^{-3}	3.3×10^{-3}	0.030	0.031	0.081	0.092	0.14	0.13
30 Dec.	7.3×10^{-3}	1.8×10^{-2}	8.9×10^{-3}	0.22	0.31	0.32	1.18	1.31	0.78

Defense through a National Defense Science and Engineering Graduate Fellowship. RAX-1 is funded by the National Science Foundation, grant ATM-0838054.

References

- [1] Blaylock, B. T., *Spacecraft Attitude Determination and Control, Magnetometers*, Kluwer Academic Publishers, Norwell, MA, 1978, pp. 180–184, Chap. 6.3.
- [2] Ripka, P., and Acuna, M. H., *Magnetic Sensors and Magnetometers, Applications of Magnetic Sensors*, Artech House, Norwood, MA, 2001, pp. 369–402, Chap. 10.
- [3] Gebre-Egziabher, D., Elkaim, G. H., Powell, J. D., and Parkinson, B. W., “Calibration of Strapdown Magnetometers in the Magnetic Field Domain,” *Journal of Aerospace Engineering*, Vol. 19, No. 2, April 2006, pp. 87–102.
doi:10.1061/(ASCE)0893-1321(2006)19:2(87)
- [4] Foster, C., and Elkaim, G., “Extension of a Two-Step Calibration Methodology to Include Nonorthogonal Sensor Axes,” *IEEE Aerospace and Electronic Systems Magazine*, Vol. 44, No. 3, July 2008, pp. 1070–1078.
doi:10.1109/TAES.2008.4655364.
- [5] Kabamba, P. T., “Course Notes for AE584: Avionics, Navigation and Guidance of Aerospace Vehicles,” Univ. of Michigan, Ann Arbor, MI, Oct. 2010, Chap.4.
- [6] van der Horn, G., and Huijsing, J. L., *Integrated Smart Sensors Design and Calibration, Measurement Errors and Correction*, Kluwer Academic Publishers, Norwell, MA, 1998, pp. 6–16, Chap. 1.4.
- [7] Alonso, R., and Shuster, M. D., “TWOSTEP: A Fast Robust Algorithm for Attitude-Independent Magnetometer-Bias Determination,” *Journal of the Astronautical Sciences*, Vol. 50, No. 4, 2003, pp. 433–451.
- [8] Alonso, R., and Shuster, M. D., “Attitude-Independent Magnetometer-Bias Determination: A Survey,” *Journal of the Astronautical Sciences*, Vol. 50, No. 4, 2003, pp. 453–475.
- [9] Alonso, R., and Shuster, M. D., “Complete Linear Attitude-Independent Magnetometer Calibration,” *Journal of the Astronautical Sciences*, Vol. 50, No. 4, 2003, pp. 477–490.
- [10] Vasconcelos, J., Elkaim, G., Silvestre, C., Oliveira, P., and Cardeira, B., “A Geometric Approach to Strapdown Magnetometer Calibration in Sensor Frame,” *IEEE Aerospace and Electronic Systems Magazine*, Vol. 47, No. 2, April 2011, pp. 1293–1306.
doi:10.1109/TAES.2011.5751259
- [11] Crassidis, J., Lai, K.-L., and Harman, R., “Real-Time Attitude-Independent Three-Axis Magnetometer Calibration,” *Journal of Guidance, Control, and Dynamics*, Vol. 28, No. 1, 2005, pp. 115–20.
doi:10.2514/1.4179
- [12] Finlay, C. C., Maus, S., Beggan, C. D., Bondar, T. N., Chambodut, A., Chernova, T. A., “International Geomagnetic Reference Field: The Eleventh Generation,” *Geophysical Journal International*, Vol. 183, No. 3, Dec. 2010, pp. 1216–1230.
doi:10.1111/j.1365-246X.2010.04804.x
- [13] Ghanbarpour Asl, H., Pourtakdoust, S., and Samani, M., “A New Nonlinear Algorithm for Complete Preflight Calibration of Magnetometers in the Geomagnetic Field Domain,” *Journal of Aerospace Engineering*, Vol. 223, No. 6, 2009, pp. 729–739.
doi:10.1243/09544100JAERO485
- [14] Acuna, M., Scheifele, J., Stella, P., Kloss, C., Smith, B., Heinshohn, G., and Sharmit, K., “Magnetic Field Cancellation Techniques for the Mars Global Surveyor Solar Array,” *Conference Record of the Twenty Fifth IEEE Photovoltaic Speciales Conference*, IEEE Publications, Piscataway, NJ, May 1996, pp. 325–8.
- [15] Baker, D. N., and Worden, S. P., “The Large Benefits of Small-Satellite Missions,” *Transactions of the American Geophysical Union*, Vol. 33, No. 33, 2008, pp. 301–312.
doi:10.1029/2008EO330001
- [16] Sandau, R., “Status and Trends of Small Satellite Missions for Earth Observation,” *Acta Astronautica*, Vol. 66, Nos. 1–2, 2010, pp. 1–12.
doi:10.1016/j.actaastro.2009.06.008
- [17] Moretto, T., and Robinson, R. M., “Small Satellites for Space Weather Research,” *Space Weather*, Vol. 6, No. 5, May 2008.
doi:10.1029/2008SW000392
- [18] Kim, E., Bang, H., and Lee, S.-H., “Attitude-Independent Magnetometer Calibration Considering Magnetic Torquer Coupling Effect,” *Journal of Spacecraft and Rockets*, Vol. 48, No. 4, 2011, pp. 691–694.
doi:10.2514/1.52634
- [19] Wolfson, R., and Pasachoff, J. M., *Physics for Scientists and Engineers*, 3rd ed., Addison Wesley Longman, Inc., Reading, MA, 1999, pp. 770–802, Chap. 30.
- [20] Crassidis, J. L., and Junkins, J. L., *Optimal Estimation of Dynamical Systems*, CRC Press, Boca Raton, FL, 2004, Sections 1.4 and 2.4.
- [21] Cutler, J., Bennett, M., Klesh, A., Bahcivan, H., and Doe, R., “The Radio Aurora Explorer: A Bistatic Radar Mission to Measure Space Weather Phenomenon,” *Proceedings of the 24th Annual Small Satellite Conference*, Utah State Univ., Logan, UT, Aug. 2010.
- [22] Cutler, J. W., Springmann, J. C., Spangelo, S., and Bahcivan, H., “Initial Flight Assessment of the Radio Aurora Explorer,” *Proceedings of the 25th Annual Small Satellite Conference*, Utah State Univ., Logan, UT, Aug. 2011.
- [23] Springmann, J. C., Sloboda, A. J., Klesh, A. T., Bennett, M. W., and Cutler, J. W., “The Attitude Determination System of the RAX Satellite,” *Acta Astronautica*, Vol. 75, June–July 2012, pp. 120–135.
- [24] Maus, S., Macmillan, S., Lowes, F., and Bondar, T., “Evaluation of Candidate Geomagnetic Field Models for the 10th Generation of IGRF,” *Earth, Planets, and Space*, Vol. 57, No. 12, 2005, pp. 1173–1181.
- [25] Springmann, J. C., “Attitude-Independent Magnetometer Calibration with Time-Varying Bias,” *Proceedings of the 25th Annual Small Satellite Conference*, Utah State Univ., Logan, UT, Aug. 2011.